An Anthropomorphic Robust Robotic Torso for Ventral and Lateral Motion with Weight Compensation

Jens Reinecke[1], Bastian Deutschmann[1], Alexander Dietrich[1], and Marco Hutter[2]

***Abstract*— The human torso is known to be highly versatile and dexterous in terms of motion capabilities and dynamic performance. Motivated by the human counterpart, we present the development of a new anthropomorphic robotic torso with comparable workspace, torques, velocities for running, and high level of mechanical robustness. In order to support large loads in ventral and lateral direction a parallel structure of actuation with tendons and a weight compensation via a spring mechanism is introduced into the system. That way, motors can be considerably downsized, which is, in turn, beneficial in terms of the dynamic characteristics of the torso. Robustness to withstand severe impacts is achieved through a clutch-based mechanism in the tendon pulleys. The entire mechanism is experimentally validated in various experiments and will be integrated as component of the compliant humanoid robot David of the DLR.**

I. INTRODUCTION

Future humanoid robotic systems are supposed to be operated in human environments, reach human-like dynamic performance, and cope with severe impacts, falls, and collisions. Thus, *robustness* becomes a more and more important feature of this next generation of robots. In this context the torso is of significant importance as it determines the whole-body dynamic capabilities of the system and it is exposed to the highest loads, similar to the human backbone.

The recent approach [1] presents a 3 DOF gravity compensation approach. The system uses a 2 DOF and 1 DOF gravity compensation mechanism in serial with two moving springs to compensate for a 3 DOF motion. Using a parallel structure it is independent of changes in the center of gravity. The mechanism offers complete compensation, but it requires a lot of building space. Another solution with reduced torque from gravitational forces is [2], where a torso is presented with 3 DOF, which features a position coupling via tendons to transmit the torque of the upper joint to the base to minimize the actuator size. Although it has 3 DOF, it does not have a lateral bending DOF. Other more anthropomorphic approaches with many DOF and actuators are presented in the following. The university of Tokyo has has longstanding experience in developing musculoskeletal humanoids, e.g Kenta, Kotaro, Kojiro, Kenzoh and Kenshiro, which aim to understand human motions by mimicking not only the skeleton-, but also the muscle arrangements. Kengoro [3] achieves human-like performance and proportions. It uses a S-shaped spine, with metal machined springs, which are specialized for each segment (cervical, thoracic and lumber) of the spine. That provides the system with crucial capabilities: highly dynamic motions, robustness and self-stabilization. It also introduces gravitational load compensation into the system. The thoracic spine is driven by eight integrated muscle modules, which are placed very similar to the human muscle arrangement.

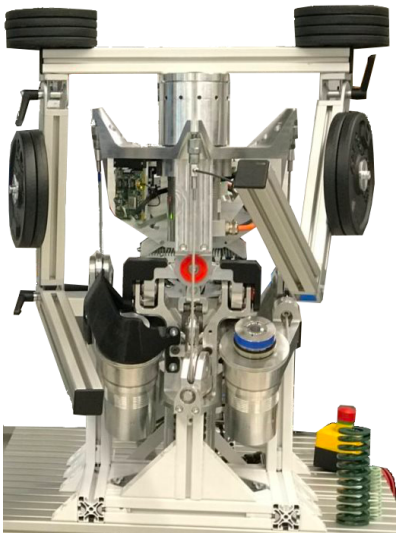

Fig. 1. Torso prototype with simplified arms for the preliminary experiments

The torso of ECCEROBOT 3 consists of five serially connected spherical joints and is actuated by 14 tendons [4]. By placing fluid-filled disks between all joints, an elastic structure is ensured to absorb shock impacts whereas the stiffness in between the first two joints is sufficiently high to pull the spine back up. Parallel mechanisms are also frequently applied in humanoid robotic torsos. The upper body of Affetto [5] utilizes a 2 degree-of-freedom (DOF) parallel mechanism driven by pneumatic actuators in combination with a revolute joint. The torso of CB^2 with 3 DOF features one parallel mechanism and two joints placed in series [6]. The parallel mechanism is utilized for roll movements and the two serial joints are used for pitch and yaw motions. The system is also pneumatically actuated which provides joint flexibility and enables the torso to absorb shocks. Furthermore, the torso of Pneumat-BS presented in [7] involves one ball and one socket joint with 3 DOF which is also actuated antagonistically by pneumatic artificial muscles/motors.

In this paper a novel 2 DOF weight compensation mech-

[1]Authors are with the Institute of Robotics and Mechatronics, German Aerospace Center (DLR), Email: jens.reinecke@dlr.de

[2]Author is with the Robotic Systems Lab, ETH Zurich, Switzerland

anism in combination with a parallel tendon setup is presented, which allows to realize similar size, robustness, and strength as the human counterpart, see Fig. 1. Instead of mimicking the complex structure of the human spine bones, discs, and muscles, the approach at hand features a lower mechatronic complexity than the above-stated works, making the torso easier to handle, easier to build and less prone to failure. The whole weight compensation mechanism [8] uses only one single spring to actuate the four motion directions of the torso: lateral left and right, ventral front and back. In consequence, smaller and faster motors can be used, which helps to approach human-like size and performance. That implies comparable strength and dynamic capabilities for running. The robustness is achieved by clutches in the pulleys. During impact, they decouple the actuators, the parallel weight compensation mechanism can consume the impact energy and the system is protected from harm. The hardware is experimentally validated on the main aspects of the prototype.

The paper is organized as follows: Section II specifies the requirements which are considered in the design process of the torso. Afterwards, the mechatronic solution is discussed in Sec. III to fullfill these requirements. The section includes the modeling of the weight compensation mechanism as well as the actuator development and design of the parallel structure. In Section IV the system is evaluated experimentally. In the last Section V the paper is summarized and future work is discussed.

II. ANALYSIS OF THE REQUIREMENTS

This section describes the human counterpart of the robotic torso, in order to provide the means to concieve the technical requirements that will be defined afterwards.

A. Physiology of the Human Torso

A total of 33 vertebrae build the spinal column, the longitudinal axis, of the human skeleton. Only 24 of them move and bend. The remaining vertebrae are fused and form the sacrum (five vertebrae) and the tailbone/coccyx (four vertebrae). The articulated vertebrae form the cervical (7), thoracic (12) and lumbar part (5). The vertebrae are separated and hold together by the cartilaginous discs, ligaments, and muscles. One functional unit consists of two discs and the inter-vertebral disc in between, the fibrocartilagnious disc absorbs shocks and increases the flexibility of the spine. The ligaments connected to the vertebral arches determine the range of motion of the spine. Together with the muscles they also improve the flexibility of the spine.

The size of the vertebrae and discs increase in downward direction of the spine due to the increased load of the body weight.

The robotic system at hand focuses on the thoracic and lumbar part of the spine. The cervical part is realized by a continuum elastic neck [9]. Therefore, only the workspace of these two parts is considered in the requirements.

B. Requirements

The requirements are classified into functional requirements (FR), minimum requirement (MR) which have to be fulfilled, and guiding requirement (GR) which serve as points of reference. The requirements are divided into main M, dimensions and workspace requirements D and task-related requirements T.

Main requirements M in Table I:
Main requirements are defined in the first step, which mainly serve as guide lines to provide underlying conditions for the designer. The requirement M.7. is set by the institute strategy to focus on electric drives.[3]

TABLE I

M.1.	FR	DOF of the torso	3
M.2.	MR	Maximum weight of the torso	40 kg
M.3.	GR	Human interaction safety	
M.4.	GR	Low design complexity	
M.5.	GR	Lightweight	
M.6.	GR	Robustness against impacts	
M.7.	GR	Electrical drives	

Dimensions and workspace requirements D in Table II:
To obtain the workspace of the spine, a person who fits the desired height and weight of the humanoid robot ($1.75\,\mathrm{m}$, $85\,\mathrm{kg}$) was measured through an external camera tracking system. Based on this set of data the workspace can be determined and a serial kinematic structure containing 3 DOF can be found which largely represents the motion capabilities of the human counterpart. An appropriate size of the torso can also be determined that way, and suitable geometric regions for the arms and legs can be derived.

TABLE II

D.1.	MR	Maximum torso height	630 ± 20 mm
D.2.	MR	Maximum torso width	410 ± 10 mm
D.3.	MR	Maximum torso depth	285 ± 30 mm
D.4.	FR	Reserved space for extremities (height)	100 mm
D.5.	FR	Ventral joint height	266 mm
D.6.	FR	Lateral joint height	287 mm
D.7.	FR	Rotational joint height	450 mm
D.8.	FR	Ventral range of motion	$-83° / +25.6°$
D.9.	FR	Lateral range of motion	$\pm 33.4°$
D.10.	FR	Rotational range of motion	$\pm 60°$

Task-related requirements T in Table III:
Additional requirements can be derived from tasks, that have been defined for the humanoid. The first one is *jogging* which yields maximum velocity requirements for all joints. The nominal stride frequency for jogging, for example, is about 1.5 Hz [10]. The second task is *holding additional weights* in different ways (in front, or on the side), the third task is *moving the upper body with stretched arms to the front* to reach for far but light objects, and the fourth task is *moving compliantly* to allow for human interaction.

[3]Please note that the use of electric drives does not imply that other drive concepts are less suitable for the considered problem.

TABLE III

T.1.	FR	Maximum running speed	10 km/h
T.2.	FR	Jogging frequency for one stride [10]	1.5 Hz
T.3.	FR	Ventral flexion during running [10]	$12 \pm 1.5°$
T.4.	FR	Lateral flexion during running [10]	$\pm 3.5°$
T.5.	GR	High energy efficiency during running/walking	
T.6.	FR	Additional load in front of the torso (upright position)	20 kg
T.7.	FR	Additional load on both sides of the torso (upright position)	40 kg
T.8.	FR	Ability to reach for far objects with stretched arms to the front	
T.9.	FR	Compliant robot control for robot and human interaction	

III. Mechatronic Design

The kinematic structure is discussed holistically for the three DOF of the torso, since the decision influences the design of the upper joint for the shoulder rotation, while the latter design parts concentrate on the ventral and lateral development.

A. Kinematic Structure

Several alternatives have been investigated with respect to the requirements in Sec. II. Possible variants are

1) Motors located directly in the joints (serial structure)
2) Full parallel setup with four linear actuators
3) Full parallel tendon setup with four motors
4) Parallel tendon setup for the ventral and lateral direction with three motors and one motor in series for the rotation

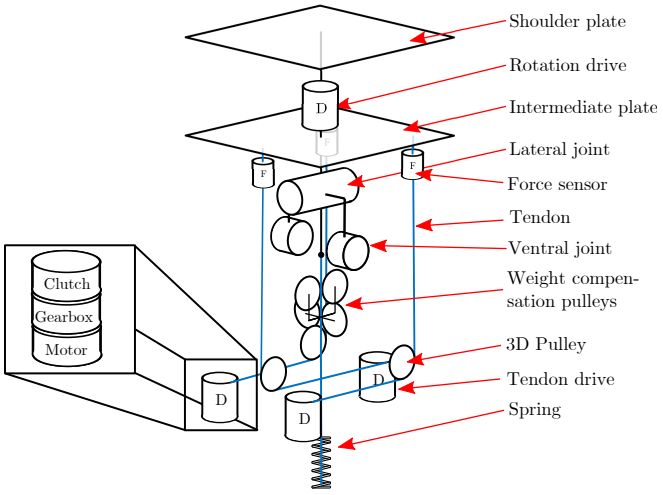

Fig. 2. Conceptual scheme of the torso

Given the joint heights defined in Table II, maximum torques and velocities for the joints were computed, which cover the desired tasks defined in Table III. For all four solutions, the equivalent actuator torques and velocities were derived to evaluate the solutions. The fourth hybrid solution is chosen due to the following reasons: High torques for bending with stretched arms require high motor-to-link-side gear ratios and rather large motors, while fast running motions require small gear ratios and smaller motors. The parallel tendon solution, where the lever arm can be chosen freely, offers the most flexible alternative for the best balance between torque and velocity. Additionally, the placement of the pulleys and actuators is very flexible, which provides the possibility to place weight compensation mechanism in the center below the joints, simplifying the tendon routing of the mechanism. The rotational axis is chosen to be serial, since it has lower maximum torques and has a high range of motion, which is difficult to reach by parallel structures for three DOF. The structure is shown in Fig. 2.

The complete valuation and decision process of the kinematic structure can be found in [11].

B. Weight Compensation

The idea is to compensate for the static torques due to gravity which are non-linear with respect to the joint angles. Numerous weight compensation methods are presented in [12], it shows the large spectrum of such mechanisms. To the best of the author's knowledge, no mechanism features a compensation with only one spring, that is capable of creating a nonlinear torque characteristic for 2 DOF. In the following the concept is shown using the equation of motion:

$$\boldsymbol{M}(\boldsymbol{q})\ddot{\boldsymbol{q}} + \boldsymbol{c}(\boldsymbol{q}, \dot{\boldsymbol{q}}) + \boldsymbol{g}(\boldsymbol{q}) = \boldsymbol{\tau}_s + \boldsymbol{\tau}_m \tag{1}$$

where $\boldsymbol{q} \in \mathbb{R}^2$ are the joint angles, $\boldsymbol{M}(\boldsymbol{q}) \in \mathbb{R}^{2\times 2}$ the inertia matrix, $\boldsymbol{c}(\boldsymbol{q}, \dot{\boldsymbol{q}}) \in \mathbb{R}^2$ the Coriolis vector, $\boldsymbol{g}(\boldsymbol{q}) \in \mathbb{R}^2$ the gravity vector and $\boldsymbol{\tau}_m \in \mathbb{R}^2$ the motor torque. The spring torque $\boldsymbol{\tau}_s \in \mathbb{R}^2$ is generated by the weight compensation mechanism. From (1), one can cancel out the gravity vector approximately:

$$\boldsymbol{g}(\boldsymbol{q}) - \boldsymbol{\tau}_s \approx \boldsymbol{0}. \tag{2}$$

To realize the nonlinear characteristics of $\boldsymbol{g}(\boldsymbol{q})$ and comply with small available space, a steel tendon is routed through the ventral and lateral joint, whereas the path of the tendon $l(\boldsymbol{q}) \in \mathbb{R}_{>0}$ changes while the mechanism is in motion, see Fig. 3. This tendon is connected to the bottom of a linear compression spring with the stiffness $k_s \in \mathbb{R}_{>0}$ which implies that, as $l(\boldsymbol{q})$ gets longer, the spring is compressed,

$$F_s(\boldsymbol{q}) = -k_s(\Delta l(\boldsymbol{q}) + x_{s,p}) \tag{3}$$

where $x_s \in \mathbb{R}$ is the spring force, $x_{s,p} \in \mathbb{R}$ is the pretension length of the spring and the relative tendon length $\Delta l(\boldsymbol{q}, h)$ is the difference between actual $l(\boldsymbol{q})$ and initial tendon length $l(\boldsymbol{q}_0)$ from the intital configuration $\boldsymbol{q}_0$. To project the spring force onto the respective joint axis, the Jacobian matrix $\boldsymbol{J}_{q,s} \in \mathbb{R}^{2x1}$ is required,

$$\boldsymbol{\tau}_s(\boldsymbol{q}) = \boldsymbol{J}_{q,s}(\boldsymbol{q})F_s(\boldsymbol{q}), \text{ with } \boldsymbol{J}_{q,s}(\boldsymbol{q}) = \left(\frac{\partial l(\boldsymbol{q})}{\partial \boldsymbol{q}}\right)^T \tag{4}$$

The kinematic arrangement that allows for the nonlinear torque profile is depicted in Fig. 3. In the following, the geometry of the tendon-path $l(\boldsymbol{q})$ is derived which is necessary to compute the spring force. To obtain the direction of

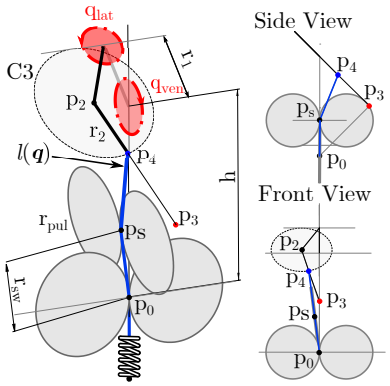

Fig. 3. Scheme of the weight compensation mechanism: Solid line grey circles are pulleys, dash-dotted red circles describe the ventral and lateral joints, and the black dashed-line circle depicts the first DOF of the cardan joint of the tendon connection from the spring to the link side, the blue line represents the configuration-dependent tendon length. We assume that the points of origin of all tendon forces can be described through single points in space. In reality, the contact point on the respective pulley will slightly move when the tendons or the link of the torso moves.

the lever r_2, which aligns with $\boldsymbol{p}_0 \in \mathbb{R}^3$, the point $\boldsymbol{p}_3$ (red point in Fig. 3) is computed by projecting the point $\boldsymbol{p}_0 \in \mathbb{R}^3$ onto the plane of the circle C3,

$$\boldsymbol{p}_3 = \boldsymbol{p}_0 - \frac{\boldsymbol{n} \cdot (\boldsymbol{p}_0 - \boldsymbol{p}_2)}{\boldsymbol{n} \cdot \boldsymbol{n}} \boldsymbol{n}, \tag{5}$$

where $\boldsymbol{n} \in \mathbb{R}^3$ is the normal vector of the plane of circle C3. Then, the intersection point $\boldsymbol{p}_4 \in \mathbb{R}^3$ (blue point in Fig. 3) is computed by intersecting the line in direction $(\boldsymbol{p}_3 - \boldsymbol{p}_2)$ with the circle C3,

$$\boldsymbol{p}_4 = \frac{r_2}{||(\boldsymbol{p}_3 - \boldsymbol{p}_2)||_2} (\boldsymbol{p}_3 - \boldsymbol{p}_2). \tag{6}$$

By rescaling the direction from $\boldsymbol{p}_0$ to $\boldsymbol{p}_4$ with the radius of the swing r_{sw}, the point $\boldsymbol{p}_s \in \mathbb{R}^3$ can be computed, which is, the point where the tendon is routed around the second pulley pair,

$$\boldsymbol{p}_s = \frac{r_{sw}}{||\boldsymbol{p}_4 - \boldsymbol{p}_0||_2} (\boldsymbol{p}_4 - \boldsymbol{p}_0), \tag{7}$$

whereas the free length of the tendon, and thus $l(\boldsymbol{q})$ result from

$$l(\boldsymbol{q}) = ||\boldsymbol{p}_4 - \boldsymbol{p}_s||^2. \tag{8}$$

The main parameter of the mechanism is the length of the lever arm, a longer arm lowers the maximum spring force so the spring size would decrease substantially. On the other hand a longer lever arm r_2 needs more space inside the torso to move into all extreme positions. Thus, the lever arm radius is limited by the design, since the whole mechanism has to fit with the ventral and lateral bearing construction inside a human-sized torso. The pulley diameter, as well as the tendon diameter are dependent on the selected spring stiffness and are computed according to optimization results. The parameters: stiffness of the spring k_s, the pretension $x_{s,p}$ and the distance h from the link connection to the pulleys are optimized. An optimization problem is solved using the 'fminsearchbnd' function from John D'Errico from File Exchange in Matlab to find these parameters whereas the scalar objective function,

$$e(\boldsymbol{q}, k_s, x_{s,p}, h) = ||\boldsymbol{g}(\boldsymbol{q}) - \boldsymbol{J}_{q,s}(k_s(\Delta l(\boldsymbol{q}, h) + x_{s,p}))||_2^2, \tag{9}$$

is minimized inside the feasible boundaries of the parameteres. Note, that in 9 the relative tendon length $\Delta l(\boldsymbol{q}, h)$ is dependent on the mechanism height h. Since the configuration of the arms can vary, $\boldsymbol{g}(\boldsymbol{q})$ is chosen in this optimization to be the gravitational torque with hanging arms. Compensating for the gravity torque with fully outstretched arms would cause an over-compensation during most motions and counteract the originally defined goal. After the optimization a spring (0R303-822D) with stiffness $61.18\,\mathrm{N/mm}$ close to the optimization solution is chosen (Table IV). A value for h close to the optimization solution is selected, and the resulting pretension $x_{s,p}$ is computed (see also Table IV). In a final step the mechanical boundaries are verified and dependent parameters are computed. The maximum spring compression $x_{s,total}$ of $56\,\mathrm{mm}$ and maximum force of $3534\,\mathrm{N}$ are not exceeded. A tendon is selected with maximum load force of $5350\,\mathrm{N}$ with the most elastic tendon configuration 8x19+7x7- strands. It is a steel tendon from Carlstahl with $3\mathrm{mm}$ diameter to keep the pulley diameter small. Since the minimum bending diameter factor of that tendon configuration is 16, we reach a pulley diameter of $48\,\mathrm{mm}$, which keeps the overall size of the mechanism small. The final result of the optimization and the error between desired torque and modeled torque created by the mechanism is shown in Fig. 4.

TABLE IV

RESULTS OF THE OPTIMIZATION AND DESIGN PROCESS

Parameter/ Constraint	Optimization	Selected Values
k_s [N/mm]	57.97	61.18
$x_{s,p}$ [mm]	29.72	27.64
h [mm]	96.6	95.0
max(F)[N]	3304	3360
$x_{s,total}$[mm]	57	55

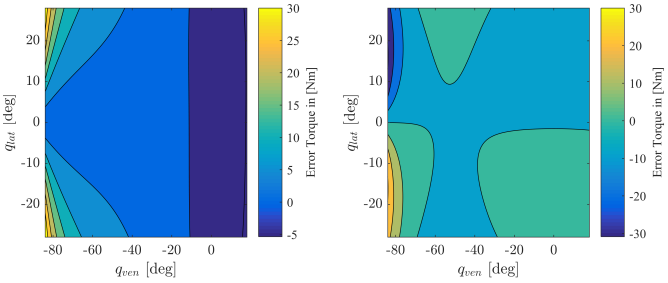

Fig. 4. Error of the ventral (left) and lateral(right) compensation. The difference between the desired gravitational torque and the torque created from the gravitational compensation mechanism

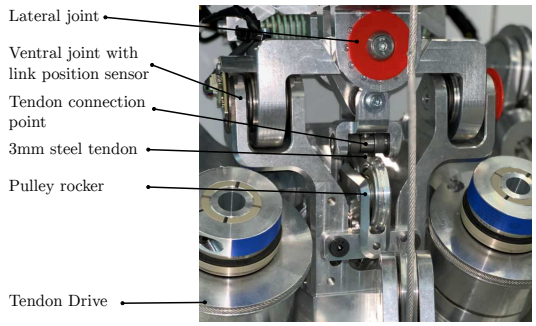

Fig. 5. Picture of the mechanism in upright configuration.

C. Actuation

The tendon actuation is of parallel structure with electrical motors. Clutches are integrated to increase the robustness of the mechanism. In the following the key components are described.

1) Pulley, Motor and Gearbox: According to the requirements T.6 – T.9 in Table III, the task with stretched arms during full ventral flexion is the most challenging one for the actuation, see also Table V (b). To provide a torque safety margin, we selected all components to reach $125\,\mathrm{Nm}$, which is $2500\,\mathrm{N}$ in the tendons. Therefore, an Ilm70x18 Robodrive hollow shaft motor from TQ-Systems in a star-parallel configuration is equipped with a CPL-25A-100 Harmonic Drive gearbox (gear ratio 100) and a pulley with a radius of $50\,\mathrm{mm}$. The pulley radius is chosen by the maximum decoupling torque of the clutch which is $135\,\mathrm{Nm}$. Thus, a maximum tendon force of $2700\,\mathrm{N}$ can be reached, which is above the desired $2500\,\mathrm{N}$ tendon force and a safety factor of 2 to the maximum load force of $5350\,\mathrm{N}$ of the tendon is kept, see also III-C.3. On the other hand, the maximum output speed of the motor of $4200\,\mathrm{rpm}$ is sufficient to move the torso with the desired jogging frequency of $1.5\,\mathrm{Hz}$ in a combined motion with $3.5\,^\circ$ lateral amplitude and a ventral amplitude of $1.5\,^\circ$, (requirements T.2 – T.4 in Table III). The complete specifications of the motor-gearbox-pulley system can found in Table VI. The cardan joint for the ventral and lateral DOF of the torso is based on tapered roller bearings from Timken (A4059/A4138-20024), which can withstand the high radial and axial loads of the ventral and lateral joint.

2) Clutches: To provide robustness the gearbox is protected by a multi-position re-engagement torque limiter of R+W (SLN). The tendon pulley is mounted on the output of the clutch, see Fig. 6. In comparison to a spring-based mechanism, this solution offers a stiff behavior for the joints in nominal state. But in the impact state, the clutch allows the parallel weight compensation mechanism to consume the impact energy, lowering the overall system stress. The clutch is based on a spring-loaded ball-lock system. The lightweight design with high reproducible decoupling torques makes it suitable for a mobile robot. If the torque reaches a mechanically adjusted threshold, the clutch will decouple. As the clutch is based on a pure mechanical system, it couples again when the torque decreased below the threshold. The selected clutch snaps back after each $30\,^\circ$ of free motion.

TABLE V

CALCULATED MAXIMUM TORQUES AND FORCES

	Initial	Max. lateral	Max. ventral	Max. ventral +arm rotation
τ_{ven} [Nm]	-2.9	-2.9	-228.8	-125.3
τ_{lat} [Nm]	0	163.5	0	99.5

(a) Joint torques in extreme positions

	Max. ventral		Max. ventral without weight comp.	
	τ[Nm]	f [N]	τ[Nm]	f [N]
left tendon	73.0	1461.0	112.3	2246.9
front tendon	0.0	0.0	0.0	0.0
right tendon	73.0	1461.0	112.3	2246.9

(b) Motor torques and tendon forces for most extreme ventral position.The tendon and actuator names derive from the main direction they pull the torso, meaning that left and right tendon pull in the lateral direction as well as if both are pulled the torso moves to the ventral extension to the back and the front tendon pulls in ventral flexion to the front.

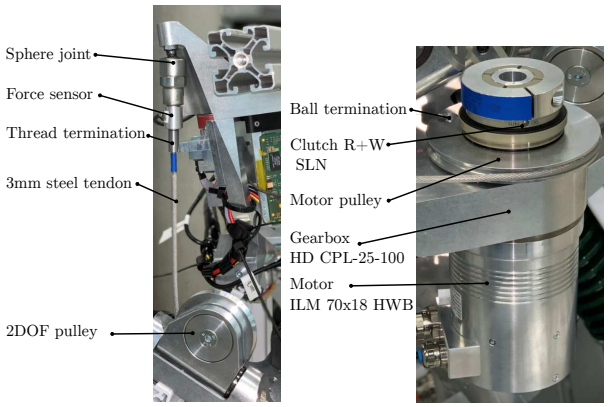

Fig. 6. Components of the actuation system next to the motors, A standard hollow-shaft Robodrive motor HWB-70x18 is used, a HD CPL-25-100-2A Gearbox, and a standard decoupling clutch SLN from R+W. To optimize design time, a stock motor is chosen, which can be replaced by an own housing design for the fully integrated system.

3) Tendons and tendon connection points: In the system a n+1 tendon actuation is chosen. The points are selected by the following constraints: no singularities in the workspace, keep the desired build space limits from constraint D.1 – D.3 in Table II, maximum tendon length change is one pulley turn to avoid specialized pulley design. The tendons utilized in the system are the same as in the weight compensation mechanism. The tendon diameter is again $3\,\mathrm{mm}$ to withstand the required maximum force $2246.9\,\mathrm{N}$, with a safety margin. As mentioned above, the selected tendons possess a large number of strings to keep pulley-diameters small. To the motor-end, a ball-termination is mounted which allows for easy maintenance, see Fig. 6. At the top end, the tendon is equipped with a thread-termination to allow for an easy connection towards the link-side force sensors, see Fig. 6. Above the force sensor, towards the mechanism, a ball-joint with a workspace of $\approx 30\,^\circ$ is mounted to avoid

TABLE VI

SPECIFICATION OF THE ACTUATORS

	Velocity	Nominal Torque/Force
Motor	4200 rpm	1.25 Nm
Gearbox	42 rpm	125 Nm
Tendon	0.2199 m/s	2500 N

tendon-buckling. In the bottom, the three tendons are routed through a two degree of freedom pulley system, see Fig. 6. Its location was optimized to create the desired torques for the motions. Due to this special routing of the tendons, the relationship between the joint-angles $\boldsymbol{q}$ and the tendon length $\boldsymbol{h}(\boldsymbol{q})$ is nonlinear and thus the projection of the tendon forces onto the generalized torques $\boldsymbol{\tau} \in \mathbb{R}^2$, known as tendon coupling matrix $\boldsymbol{P}(\boldsymbol{q}) \in \mathbb{R}^{2\times 3}$,

$$\boldsymbol{P}(\boldsymbol{q}) = \left(\frac{\partial \boldsymbol{h}(\boldsymbol{q})}{\partial \boldsymbol{q}}\right)^T, \tag{10}$$

is nonlinear as well.

D. Sensing

Two different sensory information are necessary for the control of the system. Besides the motor encoders (RLS Aksim 50), joint-position sensors in both joint axes and tendon force sensors are utilized.

1) Position Sensors: Two position encoders use the same RLS Aksim sensors as the motors and are located directly on the corresponding joint axis to measure the respective joint position $\boldsymbol{q}$ directly. Each encoder has a single-turn resolution of $18\,\mathrm{bit}$ which yields a theoretical accuracy of $\approx 0.002\,^\circ$.

2) Force Sensors: As mentioned earlier, link-sided force sensors are installed in the torso. The are located between a ball joint of the top plate and the tendon on the link side, see Fig. 6. In this way, a force control loop can be set up, on which the motor inertia as well as drive-sided friction can be reduced significantly.

Off-the-shelf force-sensors from ATP-sensors are used whereas an amplifier and AD-converter board are used to process the strain-gauge readings. The sensor-board has a theoretical resolution of $18\,\mathrm{bit}$ resulting in force resolution of $0.0077\,\mathrm{N}$.

E. Electronic and Communication Infrastructure

To understand how the different mechatronical components work together, a structural diagram is shown in Fig. 7. The supply electronics provide the different voltages needed for the inverters and the digital electronics. The power inverters are controlled by the digital electronics, which get their input over SpaceWire from a C-program running on a real-time machine. The sensors of the motors are plugged to the same digital electronics. The force sensors are plugged to an amplifier and digitizer board, which is again connected to a digital electronic. The link side position sensors are also connected, to the digital electronics. All controllers run at $3\,\mathrm{kHz}$. The controllers are designed in Matlab/Simulink® and compiled as a realtime (rt) excecutable function. When the model runs on the RT linux pc, the Simulink interface is used to control the robot, to change parameters and check the scopes.

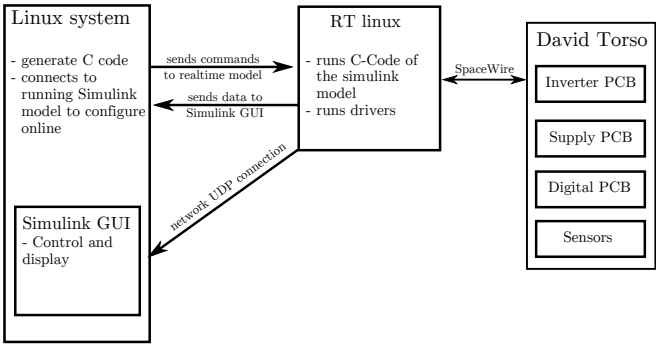

Fig. 7. System structure from the software and electronic point of view

F. Control

A basic control strategy is set up for the torso following the cascaded control structure [13]. A local force control loop is implemented for each tendon to realize the desired tendon forces $\boldsymbol{f}_{t,d} \in \mathbb{R}^3$. The control-torque $\boldsymbol{\tau}_c \in \mathbb{R}^3$ of all motors is

$$\boldsymbol{\tau}_c = \boldsymbol{E}\boldsymbol{f}_{t,d} + \boldsymbol{E}\boldsymbol{K}_t(\boldsymbol{f}_{t,d} - \boldsymbol{f}_t) \tag{11}$$

with an experimentally tuned controller gain matrix $\boldsymbol{K}_t \in \mathbb{R}^3$ and $\boldsymbol{E} \in \mathbb{R}^{2\times 2}$ diagonal matrix of the motor pulley radius r_{mot}. The outer controller of the cascaded structure realizes a desired joint-position $\boldsymbol{q}_d \in \mathbb{R}^2$ and uses the link sided position in a feedback loop to compute desired tendon forces,

$$\boldsymbol{f}_{t,d} = \boldsymbol{P}(\boldsymbol{q})^+ (\boldsymbol{K}_p(\boldsymbol{q}_d - \boldsymbol{q}) + \boldsymbol{K}_d(\dot{\boldsymbol{q}}_d - \dot{\boldsymbol{q}})) + \boldsymbol{N}(\boldsymbol{q})\boldsymbol{f}_{pre}. \tag{12}$$

Here, the tendon coupling matrix (10) is inverted $\boldsymbol{P}(\boldsymbol{q})^+$ by using the classical Moore-Penrose pseudoinversion and the null space is used to ensure that a desired pretension of the tendon-forces $\boldsymbol{f}_{pre} \in \mathbb{R}^3$ is kept, as in [13]. This is done by the statically consistent null space projector $\boldsymbol{N}(\boldsymbol{q}) \in \mathbb{R}^{3\times 3}$ from [14].

IV. EXPERIMENTAL EVALUATION

The goal of the design is to compensate for the gravitational torques arising from the weight of the upper body, to move dynamically while running and to withstand external impacts due to collisions or fall-overs. These three aspects are now discussed in experiments and are also demonstrated in the video attachment.

A. Weight Compensation

In this section the weight compensation mechanism from Section III-B is investigated. In particular, it is validated to which extent the gravitational torques are compensated by the spring mechanism. For this investigation, the torso is equipped with the equivalent weight of the envisaged arms, shoulder, neck and head ($29\,\mathrm{kg}$ in total) and is driven through the workspace using the joint position controller from Sec. III-F, with and without the weight compensation. At each static point, the tendon-forces $\boldsymbol{f}_t$ and the respective joints

angles $\boldsymbol{q}$ are recorded. These forces can, in turn, be mapped to respective torques via (10),

$$\boldsymbol{P}(\boldsymbol{q})\boldsymbol{f}_t = \boldsymbol{\tau}_t. \tag{13}$$

In the case study (without weight compensation), the gravitational torque is measured. In the second run (with weight compensation) the sum of the gravitational torque and the spring torque are measured. By subtracting the results, the created spring torque is computed . The comparison between the modeled and measured spring torque is shown in Fig. 8. It is observable that the shape of the measured and the modeled spring torque match closely with a mean error $2\,\mathrm{Nm}$ (ventral) and $5\,\mathrm{Nm}$ (lateral). In the extreme position in which the torso has already moved along the ventral direction of approximately $-83\,^\circ$and along lateral direction to the minimum and maximum position. The measured and the model spring torque diverge up to a maximal error of $12\,\mathrm{Nm}$ (ventral), and $41\,\mathrm{Nm}$ (lateral) and a minimal error of $-21\,\mathrm{Nm}$ (ventral) and $-31\,\mathrm{Nm}$ (lateral), which can be explained as follows. The model for the spring torque which is used for the design and this analysis does not consider the exact pulley kinematics, friction or sensor inaccuracies. At extreme points in the workspace, i.e. $-80\,^\circ$, the tendon surrounds the pulley and thus the model cannot represent the physics sufficiently well anymore.

B. Evaluation of Dynamic Motions

In this section the ventral and lateral direction are excited to perform jogging motions at a stride frequency of $1.5\,\mathrm{Hz}$ from the specification T.1-T.4. The robot is controlled with a sinus on the $\boldsymbol{q}_d$ with the desired frequency. Both sinuses on the ventral and lateral joint position have a phase shift of $90\,^\circ$ and the ventral position has an offset of $12\,^\circ$ to the front. For lateral motions the upper body with a total weight of $36\,\mathrm{kg}$ could reach an amplitude of $3.5\,^\circ$, while maintaining the $1.5\,^\circ$ motion in ventral direction. This shows that the requirement is accomplished. It even shows that the torso is capable of moving fast with $5.5\,^\circ$, see Fig. 9, thus higher running speeds would be possible according to [10]. The motion is also shown in the video attachment.

C. Evaluation of the Impact Behavior

To validate the robustness of the full system, a dropping experiment is conducted. The exact setup and behavior is also shown in the attached video. An impact detection is implemented to log the impact and automatically reconfigure the robot after the impact. An impact is detected by observing the difference between the tendon length measured by the motor position sensors and the estimated tendon length change from the link-side position sensor in the joints. If the difference exceeds a threshold of $3.2\,\mathrm{mm}$, an impact is assumed. This threshold is selected to be above the maximum tendon length change at $2500\,\mathrm{N}$ (nominal tendon force created by the motor see Table VI), caused by the elasticity of the steel tendon (stiffness $800\,\mathrm{N/mm}$). During the experiments, the falling height is increased until the clutch decouples, to assess the capabilities of the clutches and the reaction of the overall system. Fig. 10 shows the experimental results. At the height of $0.3\,\mathrm{m}$, the clutch decouples at $69.8\,\mathrm{Nm}(1396\,\mathrm{N})$, when setting the decoupling torque to $65\,\mathrm{Nm}$. When the tendon is disconnected, the torso moves until the clutch snaps back in after $30\,^\circ$. In the following the robot can reconfigure itself, by synchronizing its position to the link-side sensors. To select the best decoupling torque, one cannot take any possible impact into account. In a full humanoid robot numerous parameters change the impact, e.g. velocity of impact, surface compliance, number of limbs absorbing the impact, limb compliance, orientation of impact, impact load per unit area, and so on [15]. Even humans can only withstand falling accidents without severe damage by using reflexes [16]. Therefore our approach is to select a clutch setting that allows the robot to execute all the desired tasks, from the requirements analysis Sec. II-B without accidentally decoupling. At the same time, a safety margin to the maximum torque of the gearbox is kept. As a result the clutch is set to the maximum decoupling torque of $135\,\mathrm{Nm}$, which also maintains a high safety factor of 2.1 to the collision torque of the gearboxes (CPL-25-100-2A: $284\,\mathrm{Nm}$).

V. CONCLUSION AND FUTURE WORK

This paper proposes a new approach for an anthropomorphic robotic torso, using a novel weight compensation mechanism. The design and development of the parallel structure, weight compensation, and actuators are presented. That includes the model and a parameter discussion of the weight compensation to provide a basic robotic component documentation. Three experiments confirm that the developed torso meets the requirements. It shows that the novel mechanism works well in the main area of the workspace, proving the mechanism to be beneficial in terms of reduction of motor torques. The desired dynamical motions for running are feasible and comparable to human performance. The robustness capabilities are shown by impact experiments. Impact detection methods are discussed as well as the optimal setting for decoupling of the clutch. The behavior of the system to impacts is stable and crucial parts are protected during high impacts.

In the future, the current setup of the torso is extended by an additional degree of freedom to enable motions along the cranial axis. To integrate the torso into the humanoid robot DAVID, the arms, the hand, and the neck have to be mechatronically integrated. In the next step, whole body motions and fatigue experiments will be conducted to further analyze the proposed mechanism.

ACKNOWLEDGMENT

These works were supported by students in their master thesis and internships. Claudia Weiß provided the research for the biological comparison. Christopher Rheinsberg helped to develop the specifications and discussed solutions. Oemer Goecer provided dynamical simulations for the robustness and conceptual design.

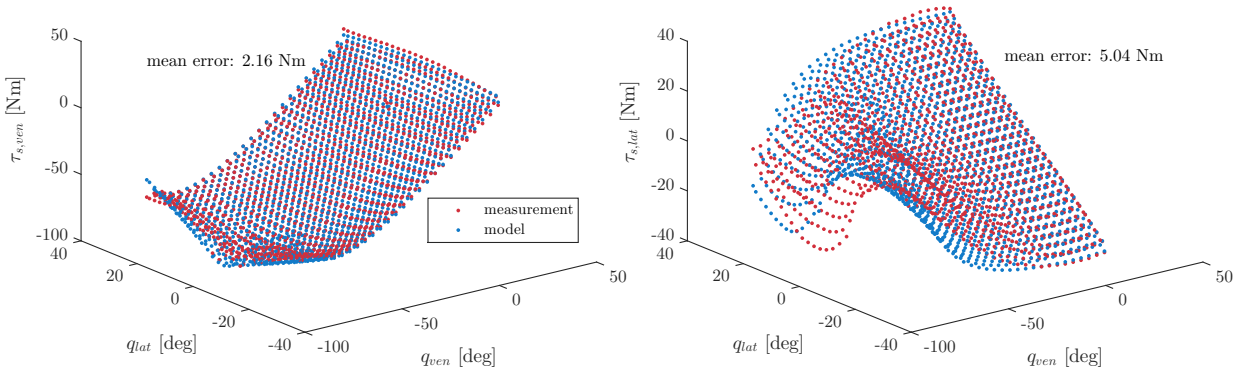

Fig. 8. Error plot of the mechanism model vs. the measurement, Left: Ventral torques, Right: Lateral torques

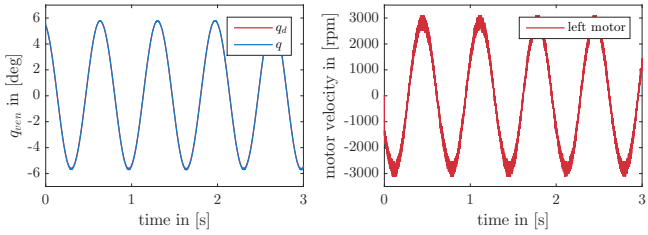

Fig. 9. Left: 5.5 ° can be reached at maximum velocity, which is more than the desired lateral motion of 3.5 °. This is necessary for the desired jogging speed requirement T.1. Right: A maximum of 3109 rpm is reached in the left motor.

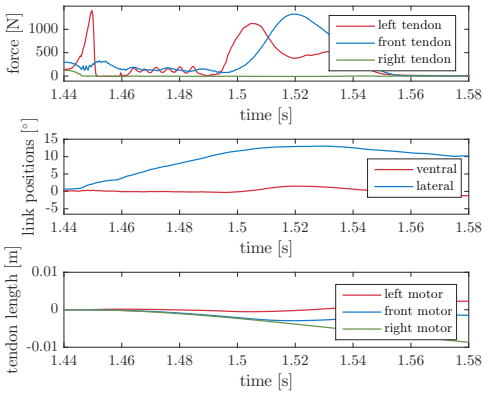

Fig. 10. Dropping experiment: a weight of 6 kg dropped on the shoulder from a height of 0.3 m, Top: The three tendon forces during the impact. The left tendon reaches the highest force up to 1396 N. The full force rises within 0.009 s. The link side notices the torso motion, which shows that the clutch decouples the tendon from the motor. Bottom: The tendon length computed from the motor position

REFERENCES

[1] S.-H. Yun, J. Seo, J. Yoon, H. Song, Y.-S. Kim, and Y.-J. Kim, "3-dof gravity compensation mechanism for robot waists with the variations of center of mass," in *2019 IEEE International Conference on Intelligent Robots and Systems (IROS)*. IEEE, 2019, pp. 3565–3570.

[2] A. Dietrich, M. Kimmel, T. Wimböck, S. Hirche, and A. Albu-Schäffer, "Workspace analysis for a kinematically coupled torso of a torque controlled humanoid robot," in *2014 IEEE International Conference on Robotics and Automation (ICRA)*. IEEE, 2014, pp. 3439–3445.

[3] Y. Asano, T. Kozuki, S. Ookubo, M. Kawamura, S. Nakashima, T. Katayama, I. Yanokura, T. Hirose, K. Kawaharazuka, S. Makino *et al.*, "Human mimetic musculoskeletal humanoid kengoro toward real world physically interactive actions," in *2016 IEEE-RAS 16th International Conference on Humanoid Robots (Humanoids)*. IEEE, 2016, pp. 876–883.

[4] A. Diamond, R. Knight, D. Devereux, and O. Holland, "Anthropomimetic robots: Concept, Construction and Modelling," *International Journal of Advanced Robotic Systems*, vol. 9, no. 209, pp. 1–14, 2012.

[5] H. Ishihara, Y. Yoshikawa, and M. Asada, "Realistic Child Robot "Affetto" for Understanding the Caregiver-Child Attachment Relationship that Guides the Child Development," *IEEE International Conference on Development and Learning*, vol. 2, pp. 1 – 5, 2011.

[6] T. Minato, Y. Yoshikawa, T. Noda, S. Ikemoto, H. Ishiguro, and M. Asada, "CB2: A Child Robot with Biomimetic Body for Cognitive Developmental Robotics," *IEEE-RAS International Conference on Humanoid Robots*, pp. 557–562, 2008.

[7] K. Ogawa, K. Narioka, and K. Hosoda, "Development of Whole-body Humanoid "Pneumat-BS" with Pneumatic Musculoskeletal System," *IEEE/RSJ International Conference on Intelligent Robots and Systems*, pp. 4838–4843, 2011.

[8] J. Reinecke, A. Dietrich, and F. Loeffl, "Robotergelenk," German Patent 102 017 203 595, 2018.

[9] J. Reinecke, B. Deutschmann, and D. Fehrenbach, "A structurally flexible humanoid spine based on a tendon-driven elastic continuum," in *Robotics and Automation (ICRA), 2016 IEEE International Conference on*. IEEE, 2016, pp. 4714–4721.

[10] A. Thorstensson, J. Nilsson, H. Carlson, and M. Zomlefer, "Trunk movements in human locomotion," *Acta Physiologica Scandinavica*, vol. 121, no. 1, pp. 9–22, 1984.

[11] O. Goecer, "Design of an Anthropomorphic Robotic Upper Body," Master Thesis, Technische Universität Muenchen, 2015.

[12] V. Arakelian, "Gravity compensation in robotics," *Advanced Robotics*, vol. 30, no. 2, pp. 79–96, 2016. [Online]. Available: https://doi.org/10.1080/01691864.2015.1090334

[13] M. Chalon, W. Friedl, J. Reinecke, T. Wimböck, and A. Albu-Schäffer, "Impedance control of a non-linearly coupled tendon driven thumb," *IEEE International Conference on Intelligent Robots and Systems*, pp. 4215–4221, 2011.

[14] A. Dietrich, C. Ott, and A. Albu-Schäffer, "An overview of null space projections for redundant, torque-controlled robots," *The International Journal of Robotics Research*, vol. 34, no. 11, pp. 1385–1400, 2015.

[15] J. M. Cameron and R. C. Arkin, "Survival of falling robots," in *Mobile Robots VI*, vol. 1613. International Society for Optics and Photonics, 1992, pp. 91–103.

[16] R. Greenwood and A. Hopkins, "Muscle responses during sudden falls in man." *The Journal of physiology*, vol. 254, no. 2, pp. 507–518, 1976.